Using shape effects to target antibody-coated nanoparticles to lung and brain endothelium

Poornima Kolhar[a,1], Aaron C. Anselmo[b,1], Vivek Gupta[b], Kapil Pant[c], Balabhaskar Prabhakarpandian[c], Erkki Ruoslahti[d,e,2], and Samir Mitragotri[a,b,2]

[a]Biomolecular Science and Engineering, and Departments of [b]Chemical Engineering and [d]Molecular Cellular and Developmental Biology, University of California Santa Barbara, Santa Barbara, CA 93106; [c]CFD Research Corporation, Huntsville, AL 35805; and [e]Sanford–Burnham Medical Research Institute, La Jolla, CA 92037

Vascular endothelium offers a variety of therapeutic targets for the treatment of cancer, cardiovascular diseases, inflammation, and oxidative stress. Significant research has been focused on developing agents to target the endothelium in diseased tissues. This includes identification of antibodies against adhesion molecules and neovascular expression markers or peptides discovered using phage display. Such targeting molecules also have been used to deliver nanoparticles to the endothelium of the diseased tissue. Here we report, based on in vitro and in vivo studies, that the specificity of endothelial targeting can be enhanced further by engineering the shape of ligand-displaying nanoparticles. In vitro studies performed using microfluidic systems that mimic the vasculature (synthetic microvascular networks) showed that rod-shaped nanoparticles exhibit higher specific and lower nonspecific accumulation under flow at the target compared with their spherical counterparts. Mathematical modeling of particle–surface interactions suggests that the higher avidity and specificity of nanorods originate from the balance of polyvalent interactions that favor adhesion and entropic losses as well as shear-induced detachment that reduce binding. In vivo experiments in mice confirmed that shape-induced enhancement of vascular targeting is also observed under physiological conditions in lungs and brain for nanoparticles displaying anti–intracellular adhesion molecule 1 and anti-transferrin receptor antibodies.

biodistribution | morphology | SMN | cylinder | drug delivery

Vascular endothelium offers a variety of therapeutic targets associated with cancer, cardiovascular diseases, inflammation, and oxidative stress (1–4). Endothelial cells overexpress adhesion molecules such as intracellular Adhesion Molecule (ICAM), vascular cell adhesion molecule (VCAM), and ʟ-selectin at inflamed sites (4–7) that may be used for targeting diseases such as myocardial infarction (8). Also, tumor neovasculature has been shown to overexpress markers such as certain integrins and prostate-specific antigens, which are nearly nonexistent on the normal vasculature surface (4, 9). In addition, collagen or von Willebrand factor on exposed vasculature offers opportunities for targeting vascular injuries (10). The search for tissue-specific markers has yielded various peptides to target local diseases (vascular zip codes) (11–13). A variety of nanoscale carriers have been synthesized to capitalize on these molecular discoveries and target drugs to diseased tissues (13, 14). However, low targeting efficacy and high off-target effects often limit the utility of these targets in therapeutic applications.

Targeting of nanoparticles to endothelium is limited by several factors. First, the target size—that is, the area of diseased endothelium—is often much smaller than that of healthy endothelium. This enhances the contribution of off-target effects and makes the choice of targeting moiety critical. Even if a highly specific targeting moiety is used, the effectiveness of nanoparticles that display these targeting moieties is often limited by their immune clearance (15, 16). The ability of particles to avoid immune clearance and accumulate at the target depends on several parameters, including size, shape, surface chemistry, and

flexibility (17–22). The role of shape in vascular dynamics has long been known in terms of its influence on the behavior of circulatory cells such as erythrocytes and platelets (23, 24). The shape of nanoparticles in the circulation is of particular interest because it has a significant impact on hydrodynamics, and interactions with vascular targets (25, 26). Here we report, using static cell cultures, microfluidics, a mathematical model, and in vivo studies in mice, that rod-shaped nanoparticles (nanorods) exhibit higher avidity and selectivity toward the endothelium compared with their spherical counterparts (Fig. 1A).

Results

Shear-Dependent Adhesion of Nanoparticles in Synthetic Microvascular Networks. Polystyrene nanospheres (200 ± 0.01 nm in diameter; Fig. 1B) and nanorods (501 ± 43.6 × 123.6 ± 13.3 nm; Fig. 1C) of equal volume were used as model particles in this study (see Table S1 for further characterization of nanoparticles). Nanorods were fabricated by the film-stretching method described previously (27). Synthetic microvascular networks (SMNs) were used to assess the interplay among shape, surface chemistry, and shear. SMNs are microfluidic channels that replicate the shear rates and flow geometries seen in physiological conditions. Through computational fluid dynamics, the shear rates at various points within the SMNs can be modeled precisely. At the same time, SMNs can incorporate key aspects of vascular physiology through establishment of an endothelial cell monolayer on their surface (see Fig. S1 for more details). For the experiments described here, SMNs were either (i) coated with ovalbumin (OVA) and exposed to particles coated with anti-OVA antibody (OVA-mAb) under flow or (ii) laden with rat brain endothelial (RBE4) cells (Fig. 1D) and exposed to anti-ICAM-1 antibody (ICAM-mAb)-coated particles under flow to mediate specific interactions between the particles and the walls of the SMNs. Particles were coated with antibodies via physical adsorption. Protein adsorption was mediated by electrostatic and hydrophobic interactions. IgG-coated particles were used as controls for nonspecific interactions. Particles were flown through the SMNs at shear rates ranging from 15 to 250 s⁻¹, which represent typical physiological shear rates observed in the microcirculation (28).

Although SMNs of any complex geometry may be used to study particle–wall interactions, plain bifurcation junctions were used in this study for simplicity. Adhesion of particles in the inlet (straight channel) as well as bifurcation junction was assessed (see SI Text for details of image analysis). Adhesion at both regions was measured because previous studies with micrometer-sized particles
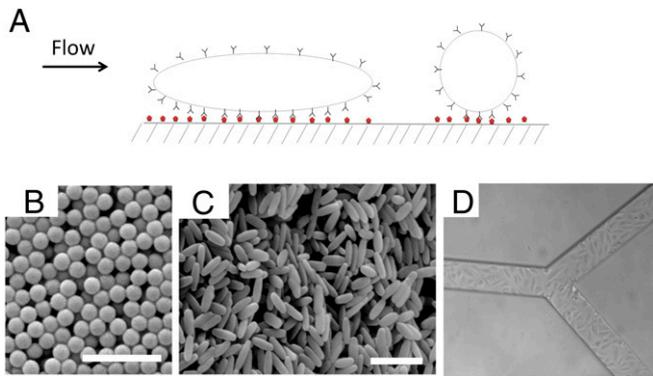
Fig. 1. Forces acting on particles under flow. (*A*) Schematic of particles interacting with a wall under flow. (*B*) Scanning electron micrographs of polystyrene spheres and (*C*) elongated particles stretched from the 200-nm spheres. Scale bar, 1 μm. (*D*) RBE4-laden SMN.

showed higher deposition in the bifurcation region than in the inlet region (26). Since the physiological microvascular region comprises numerous bifurcations, the possibility of higher particle deposition in this region was studied. For OVA-based studies, particles exhibited adhesion at the inlet region as well as at the bifurcation (Fig. 2 *A* and *B*, respectively). No significant difference was observed in particle adhesion between the inlet and the bifurcation regions. In both regions, particle adhesion decreased with increasing shear rate.

Adhesion of particles in the SMNs exhibited a peculiar interplay between shape and surface chemistry. At all shear rates, OVA-mAb–coated nanorods exhibited higher adhesion propensity than spherical particles that carried the same antibody (Fig. 2 *A* and *B*). In contrast, nonspecific IgG-coated nanorods exhibited lower adhesion than spherical particles displaying the same antibody. Thus, the difference in specific vs. nonspecific binding was higher for rods than for spheres (Fig. 2*C*). OVA-mAb–coated nanorods exhibited approximately sevenfold higher adhesion compared with IgG-coated nanorods at low shear (15 s^{-1}). The same ratio for spheres was around twofold. Even at high shear rates, the difference between the specificity of rods and that of spheres persisted. At the same time, even within the same surface chemistry, the difference between the behavior of rods and that of spheres was clear (Fig. 2*D*). Compared with IgG-coated spheres, IgG-coated rods consistently exhibited lower adhesion; whereas in the case of OVA-mAb, rods consistently exhibited higher adhesion compared with spheres.

Adhesion of Nanoparticles to Endothelial Cells in Static Cell Cultures and SMNs. To assess whether the interplay between shape and surface chemistry is also observed on cell membranes, adhesion and internalization of nanospheres and nanorods in RBE4 cells under static culture conditions were examined. ICAM-mAb–coated particles exhibited shape-dependent internalization. Specifically, after 30-min incubation, ICAM-mAb–coated nanorods were taken up to a much greater extent than ICAM-mAb–coated spheres (Fig. S2). IgG-coated nanorods, as well as IgG-coated spheres, led to significantly lower cellular uptake, and no significant
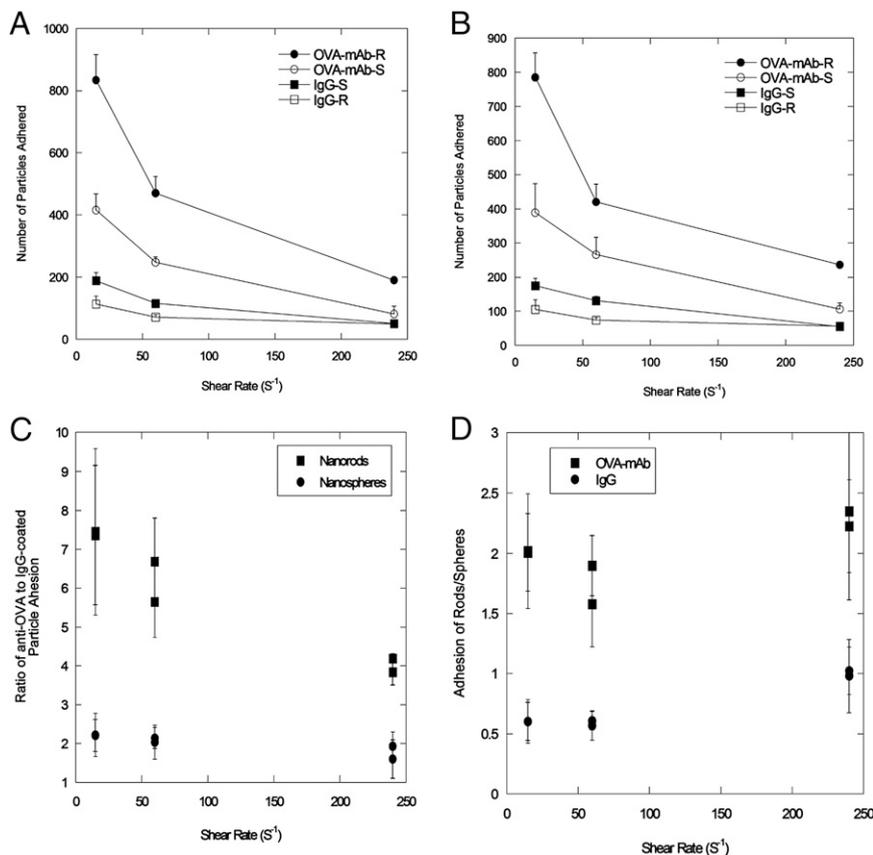
Fig. 2. Attachment of particles on OVA-coated SMNs. Quantification of attachment of particles coated with IgG [spheres (IgG-S) or rods (IgG-R)] or anti-OVA [spheres (OVA-mAb-S) or rods (OVA-mAb-R)] at various shear rates at the inlet region (*A*) and at the bifurcation (*B*) of the device. (*C*) Adhesion ratios of nanorods (■) and nanospheres (●) for specific antibodies (OVA-mAb)/nonspecific antibodies (IgG). (*D*) Adhesion ratios of OVA-mAb–coated particles (■) and IgG-coated particles (●) for nanorods and nanospheres, respectively.

differences were found between the uptake of IgG-coated nanorods and that of nanospheres.

To determine whether shape-dependent cellular adhesion and internalization are also observed under flow conditions, experiments were performed using SMNs laden with RBE4 cells (29). RBE4 cells formed confluent monolayers within the SMNs (Fig. 1D and Fig. S1). The cells were treated with 80 U/mL TNF-α to mimic inflammation and to increase ICAM-1 expression (30). Particles were allowed to flow through the SMNs at a shear rate of 60 s^{-1} for 30 min, then were imaged under the fluorescent microscope. ICAM-mAb–coated nanorods exhibited the highest attachment to the endothelial monolayer under flow conditions (Fig. 3A). ICAM-mAb–coated nanorods exhibited greater attachment/internalization than ICAM-mAb–coated spheres (Fig. 3B), IgG-coated rods, and IgG-coated spheres (Fig. 3 C and D, respectively). Detailed quantification of particle attachment to cell-laden SMNs can be seen in Fig. S3. It should be noted that spheres and rods may exhibit aggregation upon binding.

In Vivo Distribution Study of Nanoparticles in Mice. To determine whether shape-enhanced endothelial accumulation is also observed under physiological conditions, nanospheres and nanorods coated with ICAM-mAb (YN1/1.7.4) or nonspecific mouse IgG were injected intravascularly into healthy mice. Under healthy conditions, ICAM-1 is expressed at basal levels in the endothelium of the lungs (31, 32) and has been used extensively for nanoparticle targeting to the lungs (33). ICAM-mAb–coated spheres and rods exhibited higher accumulation in the lungs compared with their IgG-coated counterparts. The overall lung accumulation was about twofold higher for the ICAM-mAb rods than the ICAM-mAb spheres (Fig. 4A).The tissue distribution of ICAM-mAb–coated rods and spheres relative to their IgG-coated counterparts is shown in Fig. 4B. Liver accumulation of all particles was comparable regardless of shape or surface chemistry (Fig. 4B). Spleen accumulation was higher for nanorods than nanospheres, possibly because of high ICAM expression in the spleen and also partly because the length of the particle exceeded the maximum size necessary to avoid splenic filtration (17, 31). However, a threefold and eightfold higher

Fig. 4. In vivo biodistribution of particles. (A) Bar graph representing percentage of injected dosage per gram of organ (%ID/g) for ICAM-mAb coated rods (black), ICAM-mAb-coated spheres (dark grey), IgG-coated rods (light gray) and IgG-coated spheres (white). (B) Ratio of ICAM-mAb–coated particles to IgG-coated particles for rods (black) and spheres (gray). (C) Lung/liver accumulation of nanoparticles for IgG- or ICAM-mAb–coated spheres and rods. (D) Ratio of TfR-mAb–coated rods to spheres; the graph highlights the higher nanorod accumulation in all organs, except liver (n = 3–5 for all in vivo experiments).

lung accumulation was seen for ICAM-mAb–coated spheres and rods, respectively. ICAM-mAb nanorods exhibited preferential accumulation in the lungs compared with the liver (lung/liver ratio, ~1.6; Fig. 4C). This ratio is about 10-fold higher than that for IgG rods and twofold higher than that for ICAM-mAb spheres. Of all particles studied here, ICAM-mAb rods are the only particles that exhibited a lung/liver ratio greater than 1. Biodistribution and lung accumulation of ICAM-mAb–coated rods, as well as spheres, was dose dependent. A 100-fold increase in the dose led to about a twofold increase in lung accumulation (Fig. S4).

Shape-specific tissue accumulation was also seen for particles displaying anti-transferrin receptor antibody (TfR-mAb; Fig. 4D). TfR-mAb previously was shown to increase nanoparticle targeting to the brain (34, 35). TfR-mAb–coated rods exhibited approximately sevenfold higher accumulation in brain compared with that for TfR-mAb spheres. A lesser degree of enhancement was found in lungs, kidney, heart, and spleen (Fig. 4D). Complete biodistribution of TfR-mAb–coated nanospheres and nanorods can be seen in Fig. S5.

Discussion

This study shows that particles with a high aspect ratio increase specific attachment and reduce nonspecific attachment to their target compared with their spherical counterparts. SMNs show that specific rods (ICAM-mAb or OVA-mAb) exhibit greater adhesion than spheres with the same surface chemistry. On the other hand, IgG-coated rods exhibited less or the same adhesion than spheres with the same surface chemistry. Similar conclusions were reached in vivo. ICAM-mAb– or TfR-mAb–coated rods exhibited higher tissue accumulation than their spherical counterparts, whereas IgG-coated nanorods did not exhibit elevated

Fig. 3. Attachment of particles to endothelial cells under flow. (Top) Bright-field images showing RBE4 cells in SMNs to which particles have attached/internalized: (A) ICAM-mAb-rods, (B) ICAM-mAb-spheres, (C) IgG-rods, and (D) IgG-spheres. (Middle) Fluorescent images corresponding to the bright-field images from the top row. The images in the middle row show particles attaching/internalizing in RBE4 cells in the SMNs. (Bottom) Zoomed-in views of corresponding images from the fluorescence images from the middle row.

Kolhar et al.

tissue accumulation. Importantly, the shape effects observed in vivo are comparable, both qualitatively and quantitatively, with those seen in SMNs. The analysis of the results of this study focuses primarily on the adhesion of nanoparticles to surfaces. Particle shape is known to affect internalization by cells (36–39), and the observed accumulation in cell-laden SMNs and mice likely is affected by internalization. This study treats these contributions as a single entity, and future studies focusing on a separate assessment of these parameters (e.g., ICAM-mAbs of different binding strengths) may shed light on their individual contributions. The contribution of additional parameters, such as aspect ratios and surface charge, also should be explored.

In vivo biodistribution studies demonstrate the benefits of elongated particles in targeting the endothelium. Greater specific attachment exhibited by rod-shaped particles offers several advantages in the field of drug delivery, particularly in the delivery of drugs such as chemotherapeutics, which are highly toxic and necessitate the use of targeted approaches. The benefits of elongated particles in drug delivery were reported previously, and techniques for the mass production of different-shaped particles are being developed (40, 41). At a micrometer scale, studies have shown that elongated particles exhibit reduced phagocytosis (28, 42) and exhibit increased accumulation in lungs (22). Specifically, micrometer-scale disks were shown to exhibit longer circulation times and increased specificity of lung accumulation. They also were shown to reside longer in the prelysosomal compartment (22). The observations made in this study for nanoparticles differ in some respect from those at the micrometer scale, possibly because of the difference in the interactions with the mononuclear phagocytosis system or the time points of measurement. Filomicelles with aspect ratios between 45 and 90 have also been shown to lead to longer circulation and higher targeting (43). The longer circulation of filomicelles might have originated, in part, from their large aspect ratios, flexibility, or breakability. Other nonspherical particles, particularly discoidal particles, have been shown to exhibit up to fivefold higher tumor accumulation at a micro- and nanoscale compared with spherical particles of the same size (44). At the nanoscale, rod-shaped particles have been shown to exhibit higher cellular internalization (38) and such particles have been shown to exhibit excellent targeting in tumor xenografts (45). Iron oxide nanoworms and gold nanorods have been shown to induce higher tumor accumulation (46, 47), and gold nanorods have been shown to exhibit reduced macrophage clearance (48). Recent studies also showed the ability of rod-shaped particles to bind specifically to cancer cells in vitro (49).

The study reported here offers a systematic evaluation of the interplay between the shape and surface chemistry of nanoparticles and confirms the validity of these findings in vivo. The key finding is that rod-shaped nanoparticles exhibit increased endothelial specificity in vitro as well as in vivo. The lung/liver accumulation ratio for ICAM-mAb rods was 1.7 (compared with ~0.7 for ICAM-mAb spheres), thus confirming the increased specificity induced by particle shape. Shape-induced enhancement of targeting was also seen for TfR-mAb nanorods. The enhancement was especially prominent in the brain endothelium, which has proven to be a challenging organ to target in vivo (50). Lung accumulation of particles was dose dependent, an observation consistent with previous findings (51). Specifically, previous studies showed that a high dose of ICAM-mAb–coated particles ($>1 \times 10^{12}$ particles per animal) may lead to up to 200% ID/g accumulation in lungs. Although the doses used in the current study (5.0×10^{9} to 5.0×10^{11} particles per animal) were not as high, they did confirm the dose dependence reported in the literature (51).

The present study also confirms the utility of SMNs in studying nanoparticle–endothelium interactions in an in vivo-like setting. Adhesion and internalization of nanoparticles in endothelial cells play a critical role in determining the efficacy of targeted delivery

in various diseases, including cancer, cardiovascular diseases, and vascular injuries. Interactions of nanoparticles with the vascular endothelium are dictated by the balance between chemical affinity with the endothelial surface and the dynamics of the blood flow (52). Future studies focused on the use of chemically conjugated antibodies may offer precise control over ligand density on particle surface and may offer further insights into the interplay between shape and surface chemistry.

Blood flow affects the approach of particles toward the wall as well as the detachment of particles from the wall. Studying this complex interplay has been difficult in static cell cultures or in vivo. Although cell cultures are simple to use, they lack the contribution of fluid dynamics from the perspective of both particle–cell interactions and adaption of cells in response to shear (53). In vivo systems, although of direct relevance, suffer from the complexity of use and interference from other factors, such as immune clearance and kidney filtration. SMNs offer an optimal blend of these extremes, allowing detailed assessment of particle–cell interactions under physiologically relevant conditions. In addition, because of the small liquid volumes used, SMNs offer cost savings on consumables (54). The effect of shape and surface chemistry on nanoparticle accumulation was captured accurately by SMNs, both qualitatively and quantitatively. Although SMNs offer several advantages, they also suffer from certain limitations compared with in vivo models. Specifically, to accurately mimic the vasculature, SMN channels might be made circular in cross-section as opposed to rectangular, as used in this study. Imparting flexibility to the walls also may further help imitate the blood vessels. Additional factors associated with the nonuniform shape of blood vessels and the presence of blood cells, which will be incorporated in future studies, will affect dispersion, margination, and deposition of nanoparticles in vessels.

A mathematical model was developed to describe the shape dependence of particle–surface interactions. The model adequately captured the key underlying principles. Mathematical modeling of nanoparticle binding to cells under shear has received significant attention recently, and several excellent publications may be found in the literature that have formed the foundation of the model used here (55–57) (see *SI Text* for details). In this model, binding of nanoparticles to membranes is described here in terms of K_b, the ratio of the concentrations of surface-bound to free nanoparticles. Eq. S13 describes the relationship between K_b and the particle parameters. K_b decreases with increasing shear stress (μU), which is expected because the shear force serves to dislodge particles from the surface (first term on the right-hand side of Eq. S13). Shear-induced detachment depends on several geometrical parameters (particle aspect ratio, z, as well as particle–membrane contact area, A_c, which in turn may depend on z). Elongated particles likely will make a more substantial contact with the membrane compared with spherical particles owing to the engagement of multiple antibody–receptor bonds. Regardless of size and shape, Eq. S13 predicts that K_b decreases with increasing shear rate, an observation consistent with experimental data in Fig. 2. Eq. S13 also predicts that the enthalpic contribution associated with nanoparticle binding increases with increasing aspect ratio owing to the engagement of more antibody–receptor bonds. Eq. S13 further indicates that nanoparticle binding leads to loss of rotational and translational entropy, and the contribution of entropy loss likely increases with increasing aspect ratio.

Eq. S14 explicitly describes the relative binding of rods compared with spheres for the same surface chemistry, K^{SHAPE}, defined as the ratio of surface-bound nanorods, K_b^{ROD}, to surface–bound spheres, K_b^{SPH} $\left(K^{SHAPE} = \frac{K_b^{ROD}}{K_b^{SPH}}\right)$. In the absence of fluid flow, that is, shear rate $\dot{U} = 0$, K^{SHAPE} depends on the balance between the binding strength of the antibody (captured by the

binding enthalpy change per bond, Δh) and the entropic loss. In extreme cases—for example, when binding between the antibody and the receptor is extremely weak, that is, $\Delta h \to 0$:

$$K^{SHAPE} \ll 1. \qquad \text{[1]}$$

On the other hand, if the antibody–receptor bond is very strong—that is, $\Delta h \to -\infty$:

$$K^{SHAPE} \gg 1. \qquad \text{[2]}$$

Both predictions are consistent with the experimental data reported in this study. Fundamentally, the above equations suggest that binding of rods to the surface is hindered by the entropic loss and this loss might be compensated by the enthalpic contribution if the interactions between the antibody and the receptor are strong. This intriguing interplay between shape and selectivity may be either maintained or enhanced in the presence of flow (Figs. 2, 3C, and 4E). Future work should focus on extending the mathematical model to incorporate endocytosis as well as additional physics, such as flow alignment, particle–particle collisions, and particle–cell interactions.

The shape-induced enhancement of endothelial targeting reported here may open opportunities in vascular targeting. Rod-shaped particles may be prepared from various materials, including polymers (19), iron oxide (48), carbon nanotubes (58), DNA/PEG micelles (59), and gold (60) for applications in drug delivery. Rod-shaped particles prepared from these materials will enhance the specificity of tissue-specific targets. Various tissue-specific targets have been identified for targeting various diseases, including anti–ICAM-1 and anti-platelet endothelial cell adhesion molecule (PECAM) antibodies for inflamed endothelium (61), synthetic peptides such as RGD for tumor neovasculature (62, 63), and von Willebrand factor or platelet glycoprotein for damaged vessels or activated platelets (64). The specificity of these targeting ligands may be enhanced further by placing them on shape-engineered nanoparticles.

Materials and Methods

Fabrication of SMNs. SMNs are photolithographically designed microfluidic networks that can mimic flow patterns in physiological microvascular environments. Masters for fabricating the microchannels with a bifurcation angle of 90° and depth of 100 μm were developed using a standard photolithographic process. Sylgard 184 polydimethylsiloxane (PDMS) (Dow Corning) was prepared according to the manufacturer's instructions, poured over the developed masters in a 150-mm Petri dish, and degassed for 15 min. The polymer was then allowed to cure overnight in an oven at 65 °C to create complementary microchannels in PDMS. With a biopsy punch, through holes were made representing the inlet and outlet. The bonding surfaces of the PDMS and a precleaned 1 × 3-inch glass slide were plasma treated (200 mTorr, 18 W, 30 s) in a plasma generator (Harrick Scientific). Tygon microbore tubing with an outside diameter of 0.06 inches and inner diameter of 0.02 inches was used to connect the device to the syringe pump. Examples of the SMNs generated can be seen in Fig. S1.

Coating SMNs. The inlet port of the microfluidic device was connected to a 1-mL syringe filled with 500 μg/mL sterile OVA or fibronectin solution mounted on a programmable syringe pump (PHD 2000; Harvard Apparatus). Protein was introduced into the channel at a flow rate of 1 μL/min. After 15 min, the flow was stopped, the tubes were cut and clamped, and the device was maintained at 37 °C for 1 h or at 4 °C overnight.

Preparation and Characterization of Particles and Coating with Antibodies. Plain polystyrene (PS) particles (200 nm) were purchased from Polysciences. PS spheres were stretched into rods using the film-stretching method described by Champion et al. (27). Briefly, 10^{13} PS spheres were embedded into a polyvinyl alcohol (PVA) film (10% wt/vol in water) containing 2% (wt/vol) glycerol. Films were mounted and stretched in one dimension to three times their original length in oil at 120 °C. Rod-shaped particles were purified by centrifugation after the stretched PVA films were dissolved in a water/

isopropyl alcohol mixture. Particles at a concentration of 1 mg/mL were incubated mixed with anti-OVA or anti–ICAM-1 (eBioscience) or mouse IgG (Sigma) at a concentration of 500 μg/mL in a total volume of 100 μL in a microcentrifuge tube. The tube was left rotating at 4 °C overnight. Zeta potential (in water) was determined using the Malvern Zetasizer instrument. Protein concentration was determined using the Micro BCA assay (Pierce Biotechnology Inc.). SEM images were taken on an FEI XL40 after 120 s of palladium coating and imaged at 3–5-kV acceleration voltage at a 5-mm working distance.

Particle Adhesion in SMNs. The device was placed on the stage of an Axiovert 25 microscope (Zeiss). A 1-mL syringe was loaded with HBSS, and the device was primed at 0.1 μL/min for 5 min. Outlets of the device were immersed in a centrifuge tube filled with water to maintain a constant pressure. Antibody-coated particles were flown at shear rates of 240 s^{-1} and after 0.5 μL were flown through the device and images were taken using a cooled CCD camera (CoolSNAP HQ; Roper Scientific). The shear rate then was lowered progressively to 60 and 15 s^{-1}, with each shear rate held constant until 0.5 μL flowed through the device, and an image was taken sequentially.

Cell Culture. Immortalized RBE4 cells were cultured in alpha MEM/F10 medium supplemented with 2 mM glutamine, 100 U/mL penicillin/100 mg/mL streptomycin, 10% (vol/vol) heat-inactivated FBS, and 300 mg/mL geneticin (G418; Invitrogen). Media were changed every 3 d. For confocal studies, RBE4 cells were imaged using an inverted confocal microscope, FluoView 500 (Olympus America Inc.).

Cell Experiments in SMNs. RBE4 cells were trypsinized and resuspended in 20% FBS medium at a concentration of 2×10^7/mL. The device was perfused with medium. Cells previously were exposed to 80 U/μL of TNF-α for 12 h to ensure ICAM overexpression and mimic vasculature. Cells were seeded into the device at 8 μL/min for 30 s until the device was filled uniformly, and the tubes were cut off and clamped. The device then was placed in an incubator at 37 °C for 2–3 h, until the cells were attached and spread out. Once attached, the device was perfused with medium at 0.1 μL/min until the unattached cells were washed out. The ICAM-1– or IgG-coated particles then were resuspended in the medium at 0.125 mg/mL and flown through the device at a shear rate of 60 s^{-1} for 30 min. The device subsequently was perfused with HBSS at 60 s^{-1} for 10 min. All experiments were performed at constant shear rates to limit flow-induced changes in the cells during the binding process. The device then was imaged at 40×, and the number of particles attached to the cells was determined by image analysis.

In Vivo Experiments. Spherical and rod-shaped particles were radiolabeled with tritium (^{3}H)-oleic acid (Moravek Biochemicals). A 20% (wt/vol) particle suspension in water was added to a solution containing 100 μL ^{3}H-oleic acid, 100 μL ethanol, and 25 μL tetrahydrofuran for 30 min with constant rotation. Particles were washed 10 times at 15,000 X g for 30 min via centrifugation to remove unincorporated tritium. Rods and spheres then were coated in anti–ICAM-1 antibody (eBioscience) or anti-TfR antibody (eBioscience) at a concentration of 500 μg/mL in PBS for 1 h under constant rotation. Similarly, spheres were incubated with anti–ICAM-1 at identical concentrations. Particles then were washed two times in PBS to remove unbound protein and resuspended in saline before injection.

For biodistribution studies, 5×10^9 to 5×10^{11} radiolabeled particles were injected via tail vein into healthy female BALB/c mice (18–20 g). Six hours postinjection, the mice were anesthetized and euthanized by opening of the chest cavity and perfusion of PBS through the left ventricle. Known weights of liver, spleen, kidney, heart, lungs, and blood were harvested and incubated overnight at 60 °C in Solvable (Perkin-Elmer). The following morning, Ultima Gold (Perkin-Elmer) was added to organ solutions and organs were measured for their radioactive content in a scintillation counter. All animal protocols were approved by the Institutional Animal Care and Use Committee at the University of California, Santa Barbara.

Downloaded by guest on January 17, 2022

1. Brekken RA, Thorpe PE (2001) Vascular endothelial growth factor and vascular targeting of solid tumors. *Anticancer Res* 21(6B):4221–4229.
2. Muzykantov VR (2001) Targeting of superoxide dismutase and catalase to vascular endothelium. *J Control Release* 71(1):1–21.
3. Tousoulis D, et al. (2006) Novel therapies targeting vascular endothelium. *Endothelium* 13(6):411–421.
4. Ruoslahti E (2002) Specialization of tumour vasculature. *Nat Rev Cancer* 2(2):83–90.
5. Hanahan D, Folkman J (1996) Patterns and emerging mechanisms of the angiogenic switch during tumorigenesis. *Cell* 86(3):353–364.
6. Gallatin WM, Weissman IL, Butcher EC (1983) A cell-surface molecule involved in organ-specific homing of lymphocytes. *Nature* 304(5921):30–34.
7. Shimizu Y, Newman W, Tanaka Y, Shaw S (1992) Lymphocyte interactions with endothelial cells. *Immunol Today* 13(3):106–112.
8. Benson V, McMahon AC, Lowe HC (2007) ICAM-1 in acute myocardial infarction: A potential therapeutic target. *Curr Mol Med* 7(2):219–227.
9. Chang SS, et al. (1999) Prostate-specific membrane antigen is produced in tumor-associated neovasculature. *Clin Cancer Res* 5(10):2674–2681.
10. Ruggeri ZM (2007) Von Willebrand factor: Looking back and looking forward. *Thromb Haemost* 98(1):55–62.
11. Teesalu T, Sugahara KN, Ruoslahti E (2012) Mapping of vascular ZIP codes by phage display. *Methods Enzymol* 503:35–56.
12. Zhang L, Giraudo E, Hoffman JA, Hanahan D, Ruoslahti E (2006) Lymphatic zip codes in premalignant lesions and tumors. *Cancer Res* 66(11):5696–5706.
13. Ruoslahti E (2004) Vascular zip codes in angiogenesis and metastasis. *Biochem Soc Trans* 32(Pt3):397–402.
14. Liong M, et al. (2008) Multifunctional inorganic nanoparticles for imaging, targeting, and drug delivery. *ACS Nano* 2(5):889–896.
15. Alexis F, Pridgen E, Molnar LK, Farokhzad OC (2008) Factors affecting the clearance and biodistribution of polymeric nanoparticles. *Mol Pharm* 5(4):505–515.
16. Zolnik BS, González-Fernández A, Sadrieh N, Dobrovolskaia MA (2010) Nanoparticles and the immune system. *Endocrinology* 151(2):458–465.
17. Moghimi SM, Hunter AC, Murray JC (2001) Long-circulating and target-specific nanoparticles: theory to practice. *Pharmacol Rev* 53(2):283–318.
18. Decuzzi P, et al. (2010) Size and shape effects in the biodistribution of intravascularly injected particles. *J Control Release* 141(3):320–327.
19. Geng Y, et al. (2007) Shape effects of filaments versus spherical particles in flow and drug delivery. *Nat Nanotechnol* 2(4):249–255.
20. Merkel TJ, et al. (2011) Using mechanobiological mimicry of red blood cells to extend circulation times of hydrogel microparticles. *Proc Natl Acad Sci USA* 108(2):586–591.
21. Mitragotri S, Lahann J (2009) Physical approaches to biomaterial design. *Nat Mater* 8(1):15–23.
22. Muro S, et al. (2008) Control of endothelial targeting and intracellular delivery of therapeutic enzymes by modulating the size and shape of ICAM-1-targeted carriers. *Mol Ther* 16(8):1450–1458.
23. Wootton DM, Ku DN (1999) Fluid mechanics of vascular systems, diseases, and thrombosis. *Annu Rev Biomed Eng* 1(1):299–329.
24. Schoephoerster RT, Oynes F, Nunez G, Kapadvanjwala M, Dewanjee MK (1993) Effects of local geometry and fluid dynamics on regional platelet deposition on artificial surfaces. *Arterioscler Thromb* 13(12):1806–1813.
25. Lee SY, Ferrari M, Decuzzi P (2009) Shaping nano-/micro-particles for enhanced vascular interaction in laminar flows. *Nanotechnology* 20(49):495101.
26. Doshi N, et al. (2010) Flow and adhesion of drug carriers in blood vessels depend on their shape: A study using model synthetic microvascular networks. *J Control Release* 146(2):196–200.
27. Champion JA, Mitragotri S (2006) Role of target geometry in phagocytosis. *Proc Natl Acad Sci USA* 103(13):4930–4934.
28. Malek AM, Alper SL, Izumo S (1999) Hemodynamic shear stress and its role in atherosclerosis. *JAMA* 282(21):2035–2042.
29. Rosano JM, et al. (2009) A physiologically realistic in vitro model of microvascular networks. *Biomed Microdevices* 11(5):1051–1057.
30. Wertheimer SJ, Myers CL, Wallace RW, Parks TP (1992) Intercellular adhesion molecule-1 gene expression in human endothelial cells. Differential regulation by tumor necrosis factor-alpha and phorbol myristate acetate. *J Biol Chem* 267(17):12030–12035.
31. Hayes SH, Seigel GM (2009) Immunoreactivity of ICAM-1 in human tumors, metastases and normal tissues. *Int J Clin Exp Pathol* 2(6):553–560.
32. Yan W, et al. (2002) [Expression of intercellular adhesion molecule-1 in different organs of the mice with endotoxic shock induced by lipopolysaccharide]. *Sheng Li Xue Bao* 54(1):71–74, Chinese.
33. Muro S, et al. (2006) Endothelial targeting of high-affinity multivalent polymer nanocarriers directed to intercellular adhesion molecule 1. *J Pharmacol Exp Ther* 317(3):1161–1169.
34. Jones AR, Shusta EV (2007) Blood-brain barrier transport of therapeutics via receptor-mediation. *Pharm Res* 24(9):1759–1771.
35. Huwyler J, Wu D, Pardridge WM (1996) Brain drug delivery of small molecules using immunoliposomes. *Proc Natl Acad Sci USA* 93(24):14164–14169.
36. Doshi N, Mitragotri S (2010) Macrophages recognize size and shape of their targets. *PLoS One* 5(4):e10051.
37. Yoo JW, Mitragotri S (2010) Polymer particles that switch shape in response to a stimulus. *Proc Natl Acad Sci USA* 107(25):11205–11210.
38. Gratton SE, et al. (2008) The effect of particle design on cellular internalization pathways. *Proc Natl Acad Sci USA* 105(33):11613–11618.
39. Decuzzi P, Ferrari M (2008) The receptor-mediated endocytosis of nonspherical particles. *Biophys J* 94(10):3790–3797.
40. Glangchai LC, Caldorera-Moore M, Shi L, Roy K (2008) Nanoimprint lithography based fabrication of shape-specific, enzymatically-triggered smart nanoparticles. *J Control Release* 125(3):263–272.
41. Gratton SE, et al. (2007) Nanofabricated particles for engineered drug therapies: A preliminary biodistribution study of PRINT nanoparticles. *J Control Release* 121(1-2):10–18.
42. Champion JA, Mitragotri S (2009) Shape induced inhibition of phagocytosis of polymer particles. *Pharm Res* 26(1):244–249.
43. Shuvaev VV, et al. (2011) Endothelial targeting of antibody-decorated polymeric filomicelles. *ACS Nano* 5(9):6991–6999.
44. Godin B, et al. (2012) Discoidal porous silicon particles: Fabrication and biodistribution in breast cancer bearing mice. *Adv Funct Mater* 22(20):4225–4235.
45. Chu KS, et al. (2012) Plasma, tumor and tissue pharmacokinetics of Docetaxel delivered via nanoparticles of different sizes and shapes in mice bearing SKOV-3 human ovarian carcinoma xenograft. *Nanomedicine* 10.1016/j.nano.2012.11.008.
46. Park JH, et al. (2008) Magnetic iron oxide nanoworms for tumor targeting and imaging. *Adv Mater* 20(9):1630–1635.
47. Chauhan VP, et al. (2011) Fluorescent nanorods and nanospheres for real-time in vivo probing of nanoparticle shape-dependent tumor penetration. *Angew Chem Int Ed Engl* 50(48):11417–11420.
48. Arnida MM, Janát-Amsbury MM, Ray A, Peterson CM, Ghandehari H (2011) Geometry and surface characteristics of gold nanoparticles influence their biodistribution and uptake by macrophages. *Eur J Pharm Biopharm* 77(3):417–423.
49. Barua S, et al. (2013) Particle shape enhances specificity of antibody-displaying nanoparticles. *Proc Natl Acad Sci USA* 110(9):3270–3275.
50. Misra A, Ganesh S, Shahiwala A, Shah SP (2003) Drug delivery to the central nervous system: A review. *J Pharm Pharm Sci* 6(2):252–273.
51. Calderon AJ, et al. (2011) Optimizing endothelial targeting by modulating the antibody density and particle concentration of anti-ICAM coated carriers. *J Control Release* 150(1):37–44.
52. Decuzzi P, Lee S, Decuzzi M, Ferrari M (2004) Adhesion of microfabricated particles on vascular endothelium: A parametric analysis. *Ann Biomed Eng* 32(6):793–802.
53. Han J, et al. (2012) Acute and chronic shear stress differently regulate endothelial internalization of nanocarriers targeted to platelet-endothelial cell adhesion molecule-1. *ACS Nano* 6(10):8824–8836.
54. Prabhakarpandian B, et al. (2008) Synthetic microvascular networks for quantitative analysis of particle adhesion. *Biomed Microdevices* 10(4):585–595.
55. Decuzzi P, Ferrari M (2006) The adhesive strength of non-spherical particles mediated by specific interactions. *Biomaterials* 27(30):5307–5314.
56. Liu J, et al. (2010) Computational model for nanocarrier binding to endothelium validated using in vivo, in vitro, and atomic force microscopy experiments. *Proc Natl Acad Sci USA* 107(38):16530–16535.
57. Muzykantov VR, Radhakrishnan R, Eckmann DM (2012) Dynamic factors controlling targeting nanocarriers to vascular endothelium. *Curr Drug Metab* 13(1):70–81.
58. Bianco A, Kostarelos K, Prato M (2005) Applications of carbon nanotubes in drug delivery. *Curr Opin Chem Biol* 9(6):674–679.
59. Jiang X, et al. (2013) Plasmid-templated shape control of condensed DNA-block copolymer nanoparticles. *Adv Mater* 25(2):227–232.
60. Huang X, El-Sayed IH, Qian W, El-Sayed MA (2006) Cancer cell imaging and photothermal therapy in the near-infrared region by using gold nanorods. *J Am Chem Soc* 128(6):2115–2120.
61. Shuvaev VV, et al. (2009) Targeted detoxification of selected reactive oxygen species in the vascular endothelium. *J Pharmacol Exp Ther* 331(2):404–411.
62. Ruoslahti E, Pierschbacher MD (1987) New perspectives in cell adhesion: RGD and integrins. *Science* 238(4826):491–497.
63. Ruoslahti E (2012) Peptides as targeting elements and tissue penetration devices for nanoparticles. *Adv Mater* 24(28):3747–3756.
64. Doshi N, et al. (2012) Platelet mimetic particles for targeting thrombi in flowing blood. *Adv Mater* 24(28):3864–3869.

6 of 6 | www.pnas.org/cgi/doi/10.1073/pnas.1308345110   Kolhar et al.